JOURNAL OF PROPULSION AND POWER
Vol. 12, No. 2, March–April 1996

Vortex Shedding in Segmented Solid Rocket Motors

A. Kourta*
Institut de Mécanique des Fluides de Toulouse, F-31400 Toulouse, France

This article is devoted to the numerical simulation of vortex shedding in the field of solid-propellant rocket motors resulting from the strong coupling between the shear-layer instability and acoustic waves in the chamber. Segmented solid rocket motors tend to develop thrust and pressure oscillations, linked to a periodic vortex shedding. An axisymmetric geometry close to the realistic configuration is computed. The computer code solves the unsteady Navier–Stokes equations by means of an explicit predictor/corrector MacCormack scheme. Mesh dependence is studied by using three grid levels. In all cases, the vortex shedding process is observed. This mechanism is complex and vortex pairing occurs. The viscosity effect is analyzed by using three different viscosity values. The effect of the shape of diaphragms on vortex shedding is also studied by comparing sharp and smooth diaphragms.

I. Introduction

THIS work is part of the overall combustion stability assessment of the Ariane 5 P230 MPS solid motor and has been supported by Centre National d'Etudes Spatiales (CNES) within a research program managed by ONERA. For this motor it is believed that there exists a severe risk for instability. Occurrence of low-amplitude, sustained oscillations pulsating at a frequency associated with one or more acoustic modes of the combustion cavity affects motor performances.[1-3] One mechanism that drives pressure oscillations in rocket motors is the vortex shedding,[1,4] which can interact with the chamber acoustics to generate pressure oscillations.[5] Because of the segmented design of solid-propellant rocket motors, shear layers induced by surface discontinuities appear and produce this vortex shedding. The dipole mechanism involving the interaction of the vortices with an impingement surface can be invoked as a typical source of energy transfer from the vortex fluctuations to the acoustic field. The observed periodic vortex shedding in rocket motors[2,4] is the result of a strong coupling between the instability of mean shear flow and organ-pipe acoustic modes in the chamber. The feedback from the acoustic waves provides the control signal for the aerodynamic instability.

Because of the complexity of the problem an analytical solution to the governing equations with complex boundary conditions does not exist. Numerical simulations may provide important help for understanding the complex physics. Such simulations would naturally couple mean-flow shear layer and acoustic waves. Numerical methods have been performed to isolate and study the interaction between acoustic waves and vortex structures.[6-10] The present work is also concerned by a numerical simulation. The aim of this article is to present the ability of numerical codes to predict the unsteady behavior inside the combustion chambers of solid-propellant rocket motors and to analyze the acoustic and aerodynamic instability interaction. The computational domain corresponds to a 1/15 axisymmetric subscale motor representative of the Ariane 5 P230 solid rocket booster for which experimental results exist.[11-13] For this subscale motor, the propellant is an unmetallized analog of Ariane 5 propellant and the inhibitors are rigid metallic diaphragms that do not ablate during the firing. An experimental investigation,[11] done with various arrangements of intersegment restrictors, has brought to light the presence of naturally unstable axial modes, from the first to the sixth longitudinal mode. Among the four configurations investigated in this experiment, case A more closely corresponds to Ariane 5 P230 motor in terms of intersegment/inhibitor arrangement. The first comparison between computations and experiments for this configuration has given promising results.[12,13] The same configuration is computed in our case. A preliminary study has been developed on the numerical features of the code[14] on different configurations to show its ability to simulate vortex shedding and to predict coupling between the instability of the mean flow shear layers and the acoustic field. In this article this method is applied to this subscale motor geometry. However, the observation is restricted to axisymmetric instability as it is thought that these are dominant in this case. These mechanisms are observed at different grid levels. The viscosity (Reynolds number) effect is studied by using three different viscosity values (laminar viscosity μ_{lam}, $80\mu_{lam}$, and $400\mu_{lam}$). The flow in the solid rocket motor is turbulent and this situation requires advanced modeling for taking account of unsteadiness. As a first approximation we increase the effective viscosity to evaluate the influence of this parameter on the simulation. The organization of the flow and the properties of the vortex shedding are studied with respect to the viscosity and resonant interactions are pointed out. The nature of the diaphragms is also examined to find the differ-

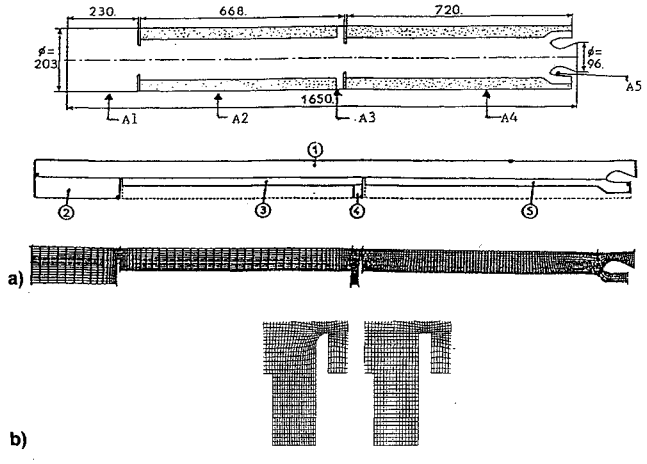

Fig. 1 Computational domain: a) geometry and mesh and b) shape of diaphragms: smooth (left) and sharp (right).

Received Nov. 5, 1994; presented as Paper 95-0727 at the AIAA 33rd Aerospace Sciences Meeting and Exhibit, Reno, NV, Jan. 9–12, 1995; revision received Oct. 3, 1995; accepted for publication Oct. 3, 1995.

*Research Scientist, Avenue du Professeur Camille Soula; also at CERFACS.

ences between the vortices induced with smooth and sharp diaphragms that depend on the position of flow separation.

In Sec. II, the numerical methodology is presented and the computational results are detailed in Sec. III.

II. Methodology

A. Governing Equations and Numerical Method

The physical model used is the full Navier–Stokes equation. This model describes conservation of mass, momentum, and total energy. These equations can be written in vector form for the axisymmetric configuration as follows:

$$\frac{\partial \boldsymbol{W}}{\partial t} + \frac{\partial \boldsymbol{F}}{\partial x} + \frac{1}{r}\frac{\partial (r\boldsymbol{G})}{\partial r} = \boldsymbol{H} \tag{1}$$

$$\boldsymbol{W} = \begin{bmatrix} \rho \\ \rho U \\ \rho V \\ \rho E \end{bmatrix} \quad \boldsymbol{F} = \begin{bmatrix} \rho U \\ \rho U^2 + \sigma_{xx} \\ \rho UV + \sigma_{xr} \\ (\rho E + \sigma_{xx})U + \sigma_{xr}V - \lambda \dfrac{\partial T}{\partial x} \end{bmatrix}$$

$$\boldsymbol{G} = \begin{bmatrix} \rho V \\ \rho UV + \sigma_{rx} \\ \rho V^2 + \sigma_{rr} \\ (\rho E + \sigma_{rr})V + \sigma_{rx}U - \lambda \dfrac{\partial T}{\partial r} \end{bmatrix} \quad \boldsymbol{H} = \begin{bmatrix} 0 \\ 0 \\ \dfrac{1}{r}(P + \sigma_{\theta\theta}) \\ 0 \end{bmatrix}$$

$$\sigma_{xx} = P - \mu\left[2\frac{\partial U}{\partial x} - \frac{2}{3}\left(\frac{\partial U}{\partial x} + \frac{1}{r}\frac{\partial rV}{\partial r}\right)\right]$$

$$\sigma_{xr} = \sigma_{rx} = -\mu\left(\frac{\partial U}{\partial r} + \frac{\partial V}{\partial x}\right)$$

$$\sigma_{rr} = P - \mu\left[2\frac{\partial V}{\partial r} - \frac{2}{3}\left(\frac{\partial U}{\partial x} + \frac{1}{r}\frac{\partial rV}{\partial r}\right)\right]$$

$$\sigma_{\theta\theta} = -\mu\left[2\frac{V}{r} - \frac{2}{3}\left(\frac{\partial U}{\partial x} + \frac{1}{r}\frac{\partial rV}{\partial r}\right)\right]$$

To close this set of equations, the pressure is related to the other state variables ρ and T, by the law of state for perfect gases.

The numerical method used is a version of the explicit MacCormack scheme.[14–16] It consists of a predictor–corrector approach. For each time step, an explicit increment is evaluated using forward or backward approximations for the inviscid part and central differences for the viscous terms.

Table 1 Mesh sizes

Block	Coarse	Medium	Fine
1	206 × 10	411 × 19	821 × 37
2	16 × 10	31 × 19	61 × 37
3	55 × 6	109 × 11	217 × 21
4	10 × 10	19 × 19	37 × 37
5	133 × 6	265 × 11	529 × 21

Table 2 Boundary conditions

Head end	No slip
Aft end	Supersonic outflow
Internal side	Symmetry
External side	A2, A4: injecting wall A1, A3, A5: no slip

B. Computational Domain

The test case computed is based on a segmented-motor model. This case is axisymmetric and requires a multiblock technique. It represents configuration A of ONERA LP3 experiment. The chosen sequence corresponds to 20 mm of burning propellant where an important instability at the third mode (900 Hz) was observed.[11–13] The meshes are designed by ONERA.[13] Three mesh levels are used (Table 1). The medium mesh is obtained from the fine one by taking every second point in each direction and the coarse one is obtained from the medium one in the same way. The geometry and the mesh are presented in Fig. 1. The configuration is divided into five blocks. The precise shape of the sharp and smooth diaphragms are also given in Fig. 1.

C. Boundary and Initial Conditions

The boundary conditions imposed are given in Table 2. A1, A2, A3, A4, and A5 are given in Fig. 1.

A no-slip condition is imposed at the inert wall where the velocity and normal pressure gradient are equal to zero. The same boundary condition is imposed along the inhibitor wall. At the injecting wall, the mass flow rate, the temperature, and zero tangential velocity are specified. For supersonic outflow classical first-order extrapolations are used.

For initial conditions computations with coarse mesh and low viscosity μ_{lam} are started from rest. The other computations are performed in sequences (e.g., the $400\mu_{\text{lam}}$ started from the $80\mu_{\text{lam}}$, the fine grid from the medium one, etc.). To evaluate the effect of the initial conditions, the case with a medium mesh and the $80\mu_{\text{lam}}$ viscosity is also computed by taking the rest as initial condition. In this case, the transient regime to reach a stationary signal is longer, but the same solution is obtained. It is concluded that the results do not depend on the initial conditions.

D. Physical Values

The physical values used are given in Table 3, where ρ_p is the propellant density, V_c is the propellant burning rate, $\dot{m}$ is the injection mass flow rate $(\rho v)_{\text{inj}}$, T_f is the flame temperature, a is the speed of sound, R is the perfect gas constant, μ is the dynamic viscosity, γ is the ratio of specific heats, and Pr is the Prandtl number.

The time steps used are $dt = 0.5 \times 10^{-6}$, 0.25×10^{-6}, and 1.0×10^{-7} s for, respectively, a coarse, medium, and fine grid. For each case 300,000 time stations have been computed to obtain a sufficiently long time interval to perform a stationary spectral analysis (Δt greater than 0.02 s). For one time step and with a coarse mesh 0.48 CPU seconds are needed on a Convex C220.

III. Computational Results

In this study three different grids (coarse, medium, and fine) are used to show mesh dependence. In fact, with a coarse mesh, the grid size can be too large, especially for low viscosity values, to resolve the boundary layer that develops at the second diaphragm where the origin of instability is located. With a coarse mesh and a low viscosity, the numerical viscosity effect on the vortex shedding mechanism can be important. To obtain a consistent analysis of the physical phenomena we need to choose the grid suitable for a given viscosity.

At all mesh levels the unsteady phenomena are observed. The amplitude and mean values are more accurate with the

Table 3 Physical values (SI units)

ρ_p	V_c	$\dot{m}$	T_f	a	R	μ	γ	Pr
1640	7.38×10^{-3}	12.1032	2700	1061.27	340.53	8.1×10^{-5}	1.225	1

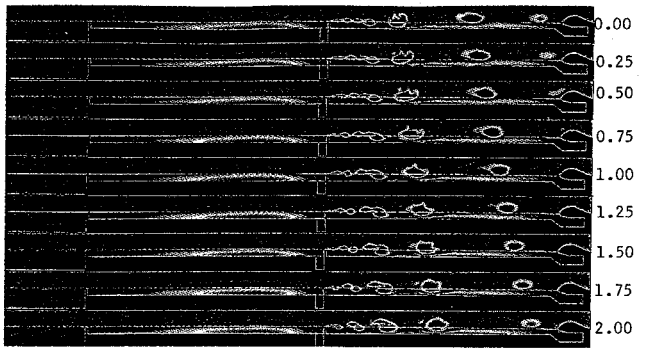

Fig. 2 Isovorticity during two periods (f = 1800 Hz) (smooth diaphragms, $80\mu_{lam}$).

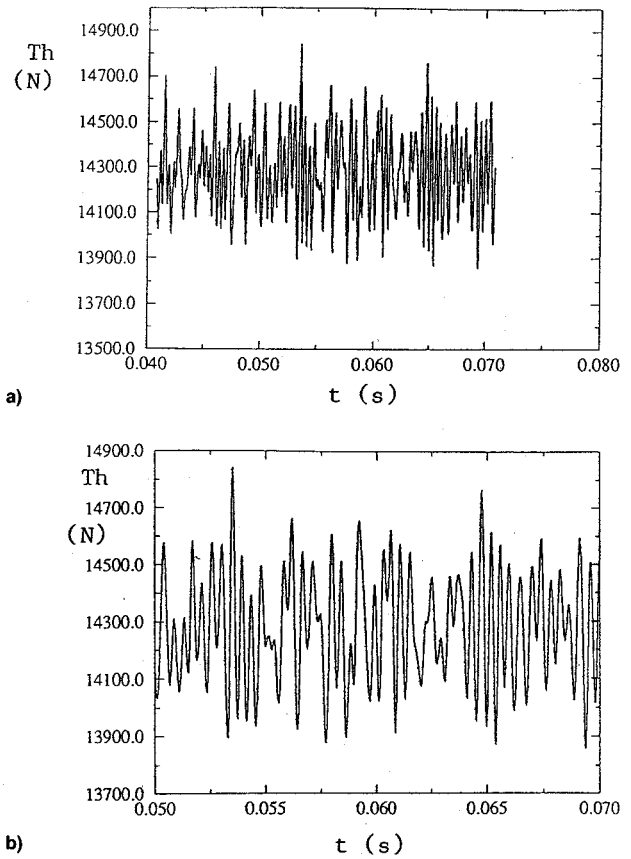

Fig. 3 Time history of the thrust (smooth diaphragms, $80\mu_{lam}$) a) complete history and b) Zoom-in ensemble.

fine mesh. The comparison done at $80\mu_{lam}$ has shown that the unsteady mechanism and corresponding frequencies are mesh dependent. At this viscosity, the best prediction is obtained with the finer mesh. The medium mesh is suitable to catch the basic phenomenon. For this reason, we use the medium mesh as a reference case to discuss the different effects of viscosity on the vortex shedding. For this mesh the best agreement with experiments will be obtained for a higher viscosity, as will be shown in the following.

First we describe the computed flow and vortex shedding mechanism in a segmented rocket motor. The effects of viscosity and the shape of diaphragms will be examined later.

To explain the features of the computed flow, we consider the case of an $80\mu_{lam}$ viscosity using the medium mesh. Figure 2 shows the isovorticity at different time stations. It can be clearly observed that the vortex shedding is captured. The formation of the vortex can be seen and a pairing mechanism takes place. The new vortex resulting from the pairing mechanism is absorbed by the nozzle. Different vortices with different sizes exist in the flow and complex nonlinear interactions can appear. Signals obtained are not monochromatic and contain complex physical phenomena.[13] Figure 3 presents the time evolution of the thrust. The velocity and pressure spectra confirm this complexity. In fact, the spectra exhibit many peaks as can be observed on Fig. 4. Frequencies detected by experiments are predicted. The axial evolution of spectra pro-

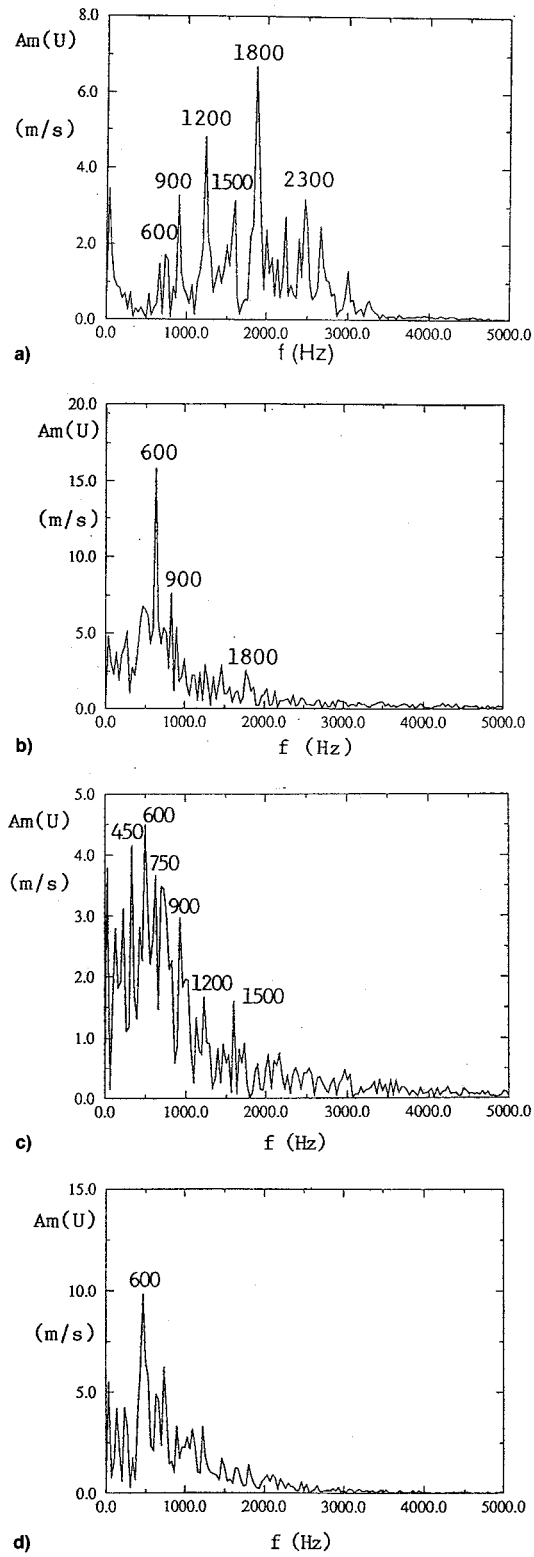

Fig. 4 Spectra of the U-component in the mixing layer (smooth diaphragms, $80\mu_{lam}$): a) x/L = 0.575, r/L = 0.025; b) x/L = 0.63, r/L = 0.025; c) x/L = 0.745, r/L = 0.025; and d) x/L = 0.86, r/L = 0.026.

Table 4 Viscosity effect: mean values (SI units)

Mean	Thrust	Phe $\times 10^{-5}$	Pae $\times 10^{-5}$	PI1 $\times 10^{-5}$	PI2 $\times 10^{-5}$
μ_{lam}	14,045	42.46	41.66	42.46	42.31
$80\mu_{lam}$	14,192	42.67	41.88	42.68	42.52
$400\mu_{lam}$	14,580	43.35	42.60	43.35	43.19

Table 5 Viscosity effect: amplitudes (SI units)

Amplitude	Thrust	Phe	Pae	PI1	PI2
μ_{lam}	401	9,340	23,306	7,611	13,251
$80\mu_{lam}$	237	8,547	18,633	7,573	11,277
$400\mu_{lam}$	51	1,815	6,643	1,348	2,776

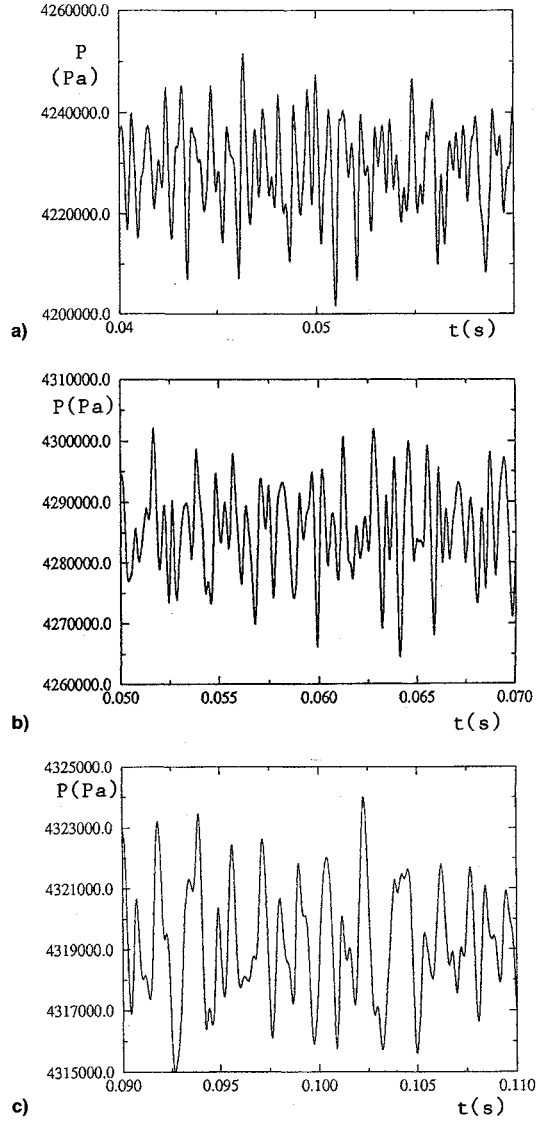

Fig. 5 Time history of the pressure (PI2) (smooth diaphragms): a) μ_{lam}, b) $80\mu_{lam}$, and c) $400\mu_{lam}$.

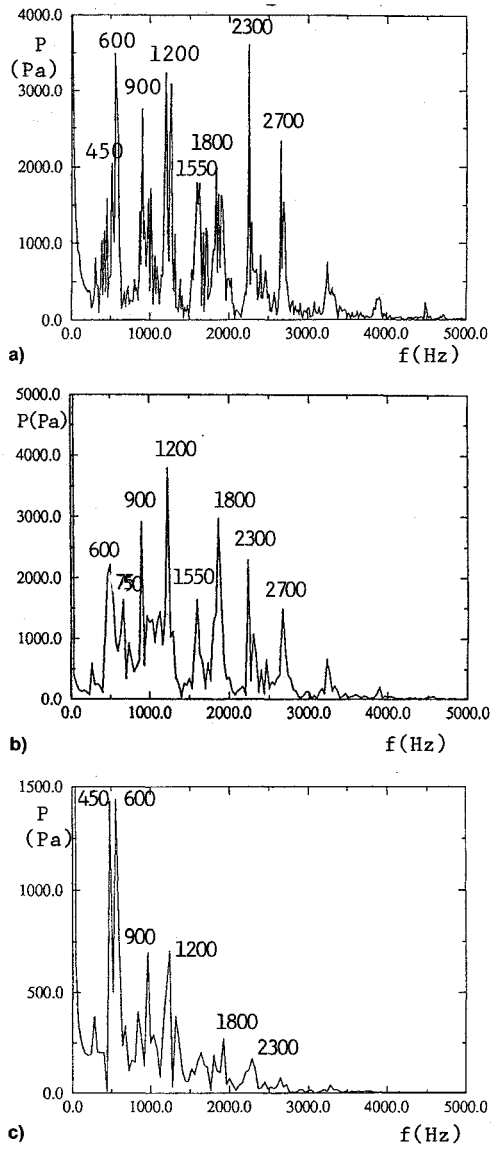

Fig. 6 Spectra of the pressure (PI2) (smooth diaphragms): a) μ_{lam}, b) $80\mu_{lam}$, and c) $400\mu_{lam}$.

vide information on the nonlinear vortex interaction. Near the shear-layer origin three dominant peaks (900, 1200, and 1800 Hz) are present (Fig. 4a). The initial rollup process is found to correspond to 1800 Hz. The peak at 900 Hz indicates a pairing of two vortices emitted at 1800 Hz. Moving downstream, peaks corresponding to pairing of two (900 Hz), three (600 Hz), or four (450 Hz) vortices emitted at 1800 Hz occur. The pairing of vortices is directly related to the development of the subharmonics.[17] It is known that the pairing mechanism constitutes one of the most striking features in the mixing-layer dynamics[18,19] and controls the space evolution of vortices. Moreover, the peaks at 750 and 1500 Hz correspond to the first and second acoustic mode of the cavity between the second diaphragm and the throat. The peak at 2300 Hz corresponds to the first acoustic mode of the head-end cavity.

The viscosity and the diaphragm shape effects are studied with the medium mesh. When the viscosity increases, the thickness of the boundary layer that develops at the second diaphragm increases and the velocity gradient at the beginning of the shear layer decreases. Hence, this shear layer becomes more stable. The viscosity strongly affects the vortex shedding and the corresponding acoustic frequencies. For the three viscosities used, the shear layer at the second diaphragm is still unstable. However, the amplitude of the instability decreases with the viscous diffusion. The mean pressures increase. Tables 4 and 5 present, respectively, the mean values and amplitudes (0-peak) of thrust, the head-end pressure (Phe), the

Table 6 Shape diaphragms effect: mean values (SI units)

Mean	Thrust	Phe $\times 10^{-5}$	Pae $\times 10^{-5}$	PI1 $\times 10^{-5}$	PI2 $\times 10^{-5}$
Smooth	14,192	42.67	41.88	42.68	42.52
Sharp	14,184	42.75	41.82	42.75	42.60

Table 7 Shape diaphragms effect: amplitudes (SI units)

Amplitude	Thrust	Phe	Pae	PI1	PI2
Smooth	237	8,547	18,633	7,573	11,277
Sharp	434	11,270	27,874	9,657	16,678

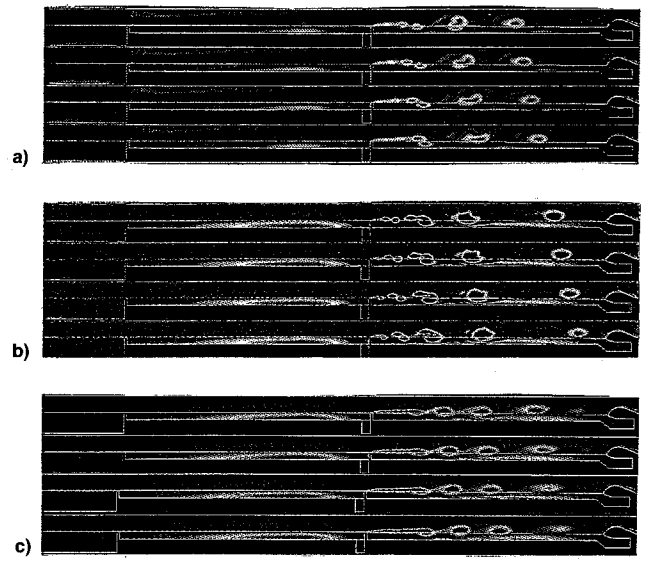

Fig. 7 Isovorticity at different time stations (smooth diaphragms): a) μ_{lam}, b) $80\mu_{lam}$, and c) $400\mu_{lam}$.

aft-end pressure (Pae), the pressure at the first diaphragm (PI1), and at the second diaphragm (PI2). The amplitude is approximated using the rms value as

$$\Delta X = \sqrt{2}\ \text{rms} = \sqrt{\frac{2}{N}\sum_{i=1}^{N}(X_i - \bar{X})^2}$$

where $\bar{X}$ is the mean value. The pressure signals at the second diaphragm for the three viscosity values are presented in Fig. 5. The smoothing effect induced by the viscosity can be observed. As the viscosity increases the amplitude decreases and the signal is more regular. The spectra corresponding to the pressure signals at the second diaphragm are plotted in Fig. 6. Among different frequencies observed in the spectra, the same peaks are detected (450, 600, 900, 1200, 1800, and 2300 Hz). The intensity of the peaks of higher frequencies decreases when the viscosity increases. The unsteady phenomena has the same origin and is related to the acoustic modes of the chamber. Among detected frequencies axial acoustic modes are observed. For example, 900 Hz is the third mode. The isovorticity contours are presented in Fig. 7. The vortex shedding mechanism is more regular at the high viscosity value. In the flowfield the pairing of vortices is only observed for the two lower viscosity cases. For these two cases the shedding frequency is 1800 Hz, corresponding to a sixth mode. However, for the case when the viscosity value is $400\mu_{lam}$, the vortex shedding corresponds to a third mode (900 Hz). For the lower viscosities, near the second diaphragm, vortices are shed in pairs and the pairing of these two vortices occurs rapidly. This new vortex corresponds to a 900-Hz frequency. When the viscosity is higher ($400\mu_{lam}$), the beginning of the vortex shedding takes place near the same position where pairing of two vortices is observed in the other

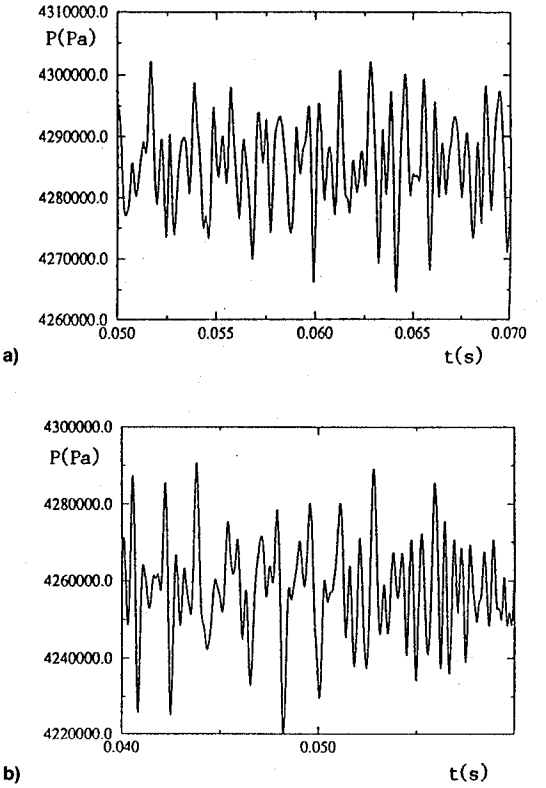

Fig. 8 Time history of the pressure (PI2) ($80\mu_{lam}$): a) smooth and b) sharp diaphragms.

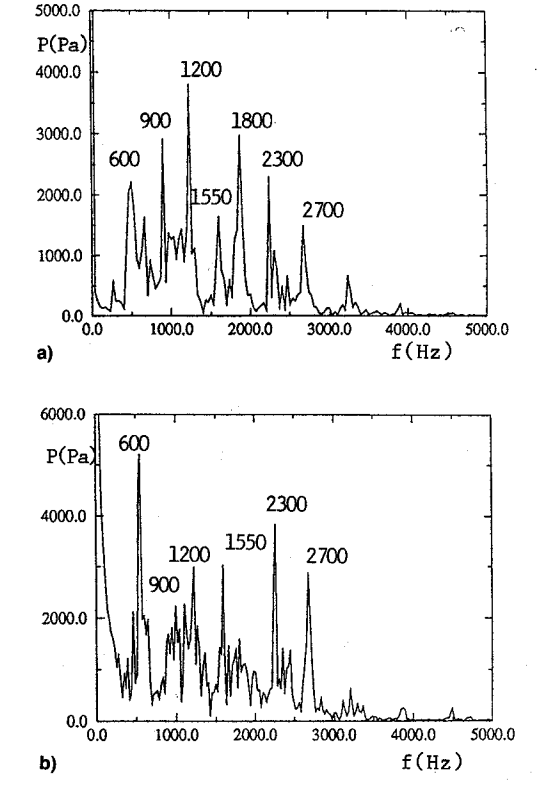

Fig. 9 Spectra of the pressure (PI2) ($80\mu_{lam}$): a) smooth and b) sharp diaphragms.

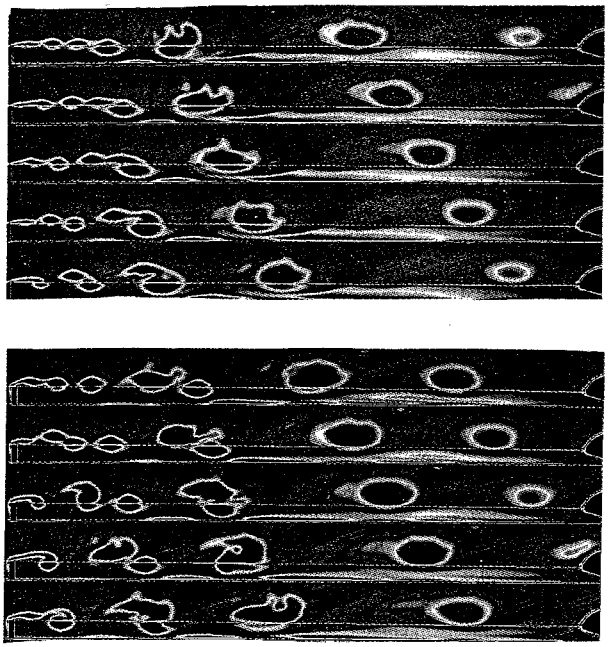

Fig. 10 Isovorticity at different time stations ($80\mu_{lam}$): a) smooth and b) sharp diaphragms.

cases. Hence, for this last case, due to the viscosity effect, the first step observed in the lower viscosity cases is missing. As observed in the experimental measurements, the 900-Hz frequency is the important one in this configuration. Moreover, frequencies of 450 and 600 Hz are present in the spectra, but in this case they do not correspond to any observed vortex pairing. Such a situation can be found in many flows for which a peak in the spectrum at a given natural or forced mode does not indicate the presence of associate vortices as it was shown for the near wake of a cylinder.[19]

In the following, smooth diaphragms are replaced by sharp ones. The medium grid and the viscosity of $80\mu_{lam}$ are used. Figure 8 shows the pressure signals at the second diaphragm for both cases. The oscillations are the same in both cases, but the amplitude is higher with the sharp diaphragms. The same remarks can be done for the other quantities as observed in Tables 6 and 7. The mean values are approximately the same (Table 6) and the amplitudes are higher with sharp diaphragms (Table 7). The spectra corresponding to the pressure signals at the second diaphragm are plotted in Fig. 9. The same peak frequencies are observed. The beginning of the separated shear layer is located upstream of the second diaphragm (Fig. 10). The instability appears earlier as does the pairing. In both cases the vortex shedding frequency is the same (1800 Hz).

IV. Conclusions

The present study has been devoted to the simulation of the vortex shedding mechanism in a rocket motor. It has shown the feasibility of the simulation of these physical mechanisms. The vortex shedding is correctly predicted and physically meaningful for sufficiently dense meshes. It is not monochromatic. The spectra display more than one frequency and its harmonics. The pairing mechanism is detected. The shedding of vortices and the pairing are the result of a strong coupling between shear-layer instabilities and acoustic motions. The frequencies detected are related to the axial acoustic modes of the rocket solid motor.

When the viscosity increases the instability amplitude decreases and the vortex shedding is more organized. For the first two cases (low and medium viscosity), the vortex shedding frequency corresponds to 1800 Hz (sixth axial mode). Vortices are shed in pairs and pairing occurs rapidly. For the highest viscosity ($400\mu_{lam}$) the vortex shedding is observed at 900 Hz (third mode) and the pairing is not detected. In this case the onset of the first vortex corresponds approximately to the position of the pairing in the lower viscosity cases. It seems to be in better agreement with the experiments.

With sharper diaphragms, the separated shear layer starts in front of the second diaphragm. In this case, the instability occurs earlier and with higher amplitude. For both the sharp and smooth diaphragms the same frequencies are observed. The vortex dynamic is not significantly modified.

Acknowledgments

This work has been supported by CNES/ONERA Contract 89/3640. We express special thanks to F. Vuillot of ONERA for his help and to H. C. Boisson for valuable comments.

References

[1]Flandro, G., "Vortex Driving Mechanism in Oscillatory Rocket Flows," *Journal of Propulsion and Power*, Vol. 3, No. 3, 1986, pp. 206–214.

[2]Brown, R., Dunlap, R., Young, S., and Waugh, R., "Vortex Shedding as a Source of Acoustic Energy in Segmented Solid Rocket," *Journal of Spacecraft and Rockets*, Vol. 8, July–Aug. 1981, pp. 312–319.

[3]Issacson, L., and Marshall, A., "Acoustic Oscillations in Internal Cavity Flows: Nonlinear Resonant Interactions," *AIAA Journal*, Vol. 20, 1982, pp. 152–154.

[4]Flandro, G., and Jacobs, H., "Vortex Generated Sound in Cavities," AIAA Paper 73-1014, Oct. 1973.

[5]Culick, F., and Magiawala, K., "Excitation of Acoustic Modes in a Chamber by Vortex Shedding," *Journal of Sound and Vibration*, Vol. 64, No. 3, 1979, pp. 455–457.

[6]Kailasanath, K., Gardner, J., and Oran, J. B. J. E., "Acoustic-Vortex Interaction and Low Frequency Oscillations in Axisymmetric Combustors," AIAA Paper 87-0165, Jan. 1987.

[7]Menon, S., and Jou, W., "Numerical Simulation of Oscillatory Cold Flows in an Axisymmetric Ramjet Combustor," *Journal of Propulsion and Power*, Vol. 6, No. 5, 1990, pp. 525–534.

[8]Menon, S., and Jou, W., "Large-Eddy Simulation of Combustion Instability in Ramjet Combustor," AIAA Paper 90-0267, Jan. 1990.

[9]Vuillot, F., and Avalon, G., "Acoustic-Mean Flow Interaction in Solid Rocket Motors Using Navier-Stokes Equations," AIAA Paper 88-2940, July 1988.

[10]Luppoglazoff, N., and Vuillot, F., "Numerical Simulation of Vortex Shedding Phenomenon in 2D Test Case Solid Rocket Motors," AIAA Paper 92-0776, Jan. 1992.

[11]Prevost, M., Traineau, J., Vuillot, F., and Caugant, C., "Experiments on 1/115 Subscale Segmented Motors," *Colloque CNES-ONERA*, Paris, Dec. 1992, pp. 6:1–30.

[12]Luppoglazoff, N., and Vuillot, F., "Simulation Numérique 2-D Instationnaire de l'Écoulement dans une Maquette à l'Echelle 1/15eme du Propulseur d'Ariane 5: Première Comparaison avec l'Expérience," *Colloque CNES-ONERA*, Paris, Dec. 1992, pp. 14:1–16.

[13]Vuillot, F., Traineau, J., Prevost, M., and Luppoglazoff, N., "Experimental Validation of Stability Assessment Methods for Segmented Solid Propellant Motors," AIAA Paper 93-1883, June 1993.

[14]Kourta, A., "Acoustic-Mean Flow Interaction and Vortex Shedding in Solid Rocket Motors," *International Journal for Numerical Methods in Fluids* (to be published).

[15]MacCormack, R., "A Numerical Method for Solving the Equations of Compressible Viscous Flow," AIAA Paper 81-0110, Jan. 1981.

[16]MacCormack, R., "Current Status of Numerical Solutions of the Navier-Stokes Equations," AIAA Paper 85-0032, Jan. 1985.

[17]Ho, C., and Huerre, P., "Perturbed Free Shear Layers," *Annual Review of Fluid Mechanics*, No. 16, 1984, pp. 365–424.

[18]Kourta, A., Braza, M., Chassaing, P., and HaMinh, H., "Numerical Analysis of a Natural and Excited Two-Dimensional Mixing Layer," *AIAA Journal*, Vol. 25, No. 2, 1987, pp. 279–286.

[19]Kourta, A., Boisson, H., Chassaing, P., and HaMinh, H., "Nonlinear Interaction and Transition to Turbulence in the Wake of a Circular Cylinder," *Journal of Fluid Mechanics*, Vol. 181, 1987, pp. 141–161.